

ASCA VIEW OF THE SUPERNOVA REMNANT γ CYGNI (G78.2+2.1) :
BREMSSTRAHLUNG X-RAY SPECTRUM FROM LOSS-FLATTENED ELECTRON
DISTRIBUTION

Y. UCHIYAMA,^{1,2} T. TAKAHASHI,^{1,2} F.A. AHARONIAN,³ AND J.R. MATTOX⁴
Draft version November 8, 2018

ABSTRACT

With the *ASCA* X-ray satellite, we perform spatial and spectral studies of the shell-type supernova remnant (SNR) γ Cygni that is associated with the brightest EGRET unidentified source 3EG J2020+4017. At energies below 3 keV the bulk of the X-ray flux from the remnant is well described by the emission of thermal plasma with characteristic temperature $kT_e \simeq 0.5\text{--}0.9$ keV. In addition to this thermal emission, we found an extremely hard X-ray component from several clumps localized in the northern part of the remnant. This component, which dominates the X-ray emission from the remnant above 4 keV, is described by a power-law with a photon index of $\Gamma \simeq 0.8\text{--}1.5$. Both the absolute flux and the spectral shape of the nonthermal X-rays cannot be explained by the synchrotron or inverse-Compton mechanisms. We argue that the unusually hard X-ray spectrum can be naturally interpreted in terms of nonthermal bremsstrahlung from Coulomb-loss-flattened electron distribution in dense environs with the gas density about 10 to 100 cm^{-3} . For given spectrum of the electron population, the ratio of the bremsstrahlung X- and γ -ray fluxes depends on the position of the ‘‘Coulomb break’’ in the electron spectrum. Formally, the entire high energy γ -ray flux detected by EGRET from γ Cygni could originate in the hard X-ray regions. However, it is more likely that the bulk of γ -rays detected by EGRET come from the radio-bright and X-ray dim cloud at southeast, where the very dense gas and strong magnetic field would illuminate the cloud in the radio and γ -ray bands, but suppress the bremsstrahlung X-ray emission due to the shift of the ‘‘Coulomb break’’ in the electron spectrum towards higher energies.

Subject headings: acceleration of particles—cosmic rays— radiation mechanisms:non-thermal—shock waves— supernova remnants

1. INTRODUCTION

The origin of the unidentified EGRET γ -ray sources in the Galactic plane has been puzzling since their discovery. The third EGRET catalog (Hartman et al. 1999) lists 57 unidentified sources at low Galactic latitude ($|b| \leq 10^\circ$). Rotation-powered pulsars are likely to account for part of these GeV γ -ray sources; five pulsars have been detected at GeV energies to date. Another possible origin for some of the unidentified sources is the emission from accelerated cosmic-rays at the shock of shell-type supernova remnants (SNRs). It is reported that the probability to find EGRET unidentified sources in the vicinity of shell-type SNRs is significantly high (Sturmer & Dermer 1995). Although the relatively young SNRs, being in their Sedov phase, are natural sites of high energy γ -ray production through electron bremsstrahlung and hadronic interactions, it has been recognized that in most cases the expected γ -ray fluxes at MeV/GeV energies are too low to be detected by EGRET (Drury, Aharonian, & Völk 1994). However, the γ -ray fluxes can be dramatically enhanced in SNRs having dense gas environments, e.g., in large molecular clouds overtaken by supernova shells (Aharonian, Drury, & Völk 1994). Remarkably, among the SNRs possibly detected by EGRET are the radio-bright and nearby objects γ Cygni, IC 443, W44, and W28 (Esposito et al. 1996) that are all associated with molecular clouds. The recent searches for SNRs in the vicinity of some of the unidenti-

fied EGRET sources revealed new evidence of γ -ray emission from ‘‘supernova remnant–molecular cloud’’ interacting systems (Combi, Romero, & Benaglia 1998; Combi et al. 2001). If gamma-rays of such systems have hadronic origin, and the acceleration of protons extends to 10 TeV and beyond, the TeV γ -ray emission from these objects should be detectable also by current ground-based detectors (Aharonian, Drury, & Völk 1994). At energies below the threshold of production of π^0 -decay γ -rays around 70 MeV, the electron bremsstrahlung remains the only noticeable γ -ray production process. Therefore, the detection of γ -rays by EGRET down to several tens of MeV implies the existence of low-energy (< 100 MeV) electrons in these objects. The best information about higher energy electrons, typically between 1 and 10 GeV electrons, is provided by the synchrotron radio emission at GHz frequencies.

The accelerated electrons produce also nonthermal X-rays through the synchrotron radiation and the bremsstrahlung. Both channels contain unique information about the nonthermal electron populations at extremely high (multi-TeV), and very low (sub-MeV) energies, respectively. Thus, the X-ray observations may help to reveal the nature of the unidentified EGRET sources that are associated with SNRs by looking for ultrarelativistic and subrelativistic electrons, and probing the environments of the remnants.

The γ Cygni (G78.2+2.1) SNR has a clear position-

¹ Institute of Space and Astronautical Science, 3-1-1 Yoshinodai, Sagami-hara, Kanagawa 229-8510, Japan; uchiyama@astro.isas.ac.jp

² Department of Physics, University of Tokyo, 7-3-1 Hongo, Bunkyo-ku, Tokyo 113-0033, Japan

³ Max-Planck-Institut für Kernphysik, Postfach 103980, D-69029 Heidelberg, Germany

⁴ Department of Physics & Astronomy, Francis Marion University, Florence, SC 29501-0547

correlation with the brightest unidentified γ -ray source 3EG J2020+4017. It is a nearby (1–2 kpc) shell-type SNR with the radio shell of $\sim 60'$ diameter (Higgs et al. 1977). The radio flux density of 340 Jy at 1 GHz ranks it as the fourth brightest SNR in the sky at this frequency (Green 2000). Almost 60% of the radio flux comes from southeastern part which has been known as DR4 (Downes & Rinehart 1966). The spectral index of the radio spectrum averaged over the whole remnant is measured as $\alpha \simeq 0.5$ (Green 2000). Its variation across the remnant is as small as $\Delta\alpha \sim \pm 0.15$ (Zhang et al. 1997). The EGRET source has the steady flux of $F(E > 100 \text{ MeV}) = (12.6 \pm 0.7) \times 10^{-7} \text{ photons cm}^{-2}\text{s}^{-1}$ and a best-fit power-law index of 2.07 ± 0.05 (Esposito et al. 1996). Prior to the EGRET detection, γ -ray source 2CG078+2 was detected in the vicinity of γ Cygni with the *COS-B* satellite (Pollock 1985). Despite extensive searches for TeV γ -ray emission, significant excesses have not been detected (Buckley et al. 1998). Since a simple extrapolation of the EGRET flux exceeds the Whipple upper limit by an order-of-magnitude, the spectrum must have a cutoff or steepen well below the TeV energy (Gaisser, Protheroe, & Stanev 1998; Buckley et al. 1998).

Presented here are the results from and implications of *ASCA* observations of the γ Cygni SNR. Of particular interest is the discovery of hard X-ray emission localized to the northern part of γ Cygni. The plan of this paper is as follows. The *ASCA* observations are briefly summarized in §2. We perform the X-ray image analysis in §3.1 and the spectral fits in §3.2. In §4.2, we interpret the soft X-ray data in terms of shock–cloud interaction. The origin of the hard X-ray emission is discussed in §4.3.

2. OBSERVATIONS

We performed *ASCA* observations of γ Cygni SNR twice in 1996 and 1997. The northern part of the remnant was observed for 40 ks in 1996 May. Observations were carried out in 1997 May with three pointings toward the north, south, and east of γ Cygni with 60, 16, and 12 ks duration, respectively. The data from two Gas Imaging Spectrometer (GIS; Makishima et al. 1996) detectors were acquired in the standard pulse-height mode. Two Solid-state Imaging Spectrometer (SIS; Burke et al. 1994) detectors were operated in 4-CCD mode. Each detector is coupled to its own telescope with nested conical foil mirrors. Once combined all observations, field of view (FOV) of GIS covers almost all part of the remnant.

The data from the detectors were screened by standard procedures, except for the strict rise-time screening in the GIS analysis, because of the mode we chose for the operation. The observed count rate for the north of γ Cygni was 0.57 (0.59) counts/s within a central $20'$ radius in the 0.7–10 keV energy band with GIS2 (GIS3). The degradation of the SIS performance due to the accumulated radiation damage in orbit is found to be substantial in our data. Even for the data taken with faint mode, in which RDD (Residual Dark Distribution) correction can be applied, the spectral resolution of SIS is found to be of no advantage to that of GIS. In addition, the smaller effective area at high energies and the narrower FOV for SIS than those for GIS do not serve our purpose. The results presented in this paper are from the GIS data.

3. DATA ANALYSIS AND RESULTS

3.1. X-ray Images

The *ASCA* GIS data for the four pointings were combined to construct the X-ray images in selected energy bands. We discard the data outside the central region of the detector with a radius greater than $20'$. By utilizing the night-earth observation data set, we subtract the instrumental background from each pointing data. Since we did not obtain the rise-time information, the normalization of the background image is increased by 30% as compared with the nominal case. The background-subtracted images are combined with corrections for the exposure time and the vignetting effects. Finally the images are smoothed with a function comprised of a narrow core ($\lesssim 1'$) and a broad wing to simulate the point spread function (PSF) of the telescope. Figure 1*a*, 1*b*, and 1*c* show the resultant X-ray images in 0.7–1 keV (soft), 1–3 keV (medium), and 4–7 keV (hard) energy bands, respectively.

We find strikingly different appearance of the SNR in these energy bands. In the soft band image, clumpy sources appear at north and limb-brightened emission is seen at south. The medium image shows widespread emission distributed from north to southeast, in addition to the southern bright shell. In the hard energy band, several clumpy sources in the north region stand out dramatically (Figure 1*c*). Hereafter, we refer to the clump centered at a celestial coordinate (J2000) of $R.A. = 20^{\text{h}}21^{\text{m}}12^{\text{s}}$, $decl. = 40^{\circ}47'55''$ as C1 and the other one at $R.A. = 20^{\text{h}}20^{\text{m}}00^{\text{s}}$, $decl. = 40^{\circ}40'03''$ as C2. Since another hard source C3 is located at the western edge of the FOV, we do not report a spectral study of C3 in this paper.

The hard source C2 appears to be extended by a few arcminutes. In order to evaluate quantitatively, we compared the count rate profile centered on the clump C2 with the detector PSF in the 3–10 keV band, as plotted in Figure 2. The background level shown there is taken from the southern part of the remnant. It is obvious that the hard X-ray emission extends up to $4'$ – $6'$ beyond the radial profile of a single point source. In Figure 2, we also plot the simulated profile of a circular source which has uniform surface brightness with a radius of $4'$ centered on C2. On the other hand, we obtain no sign of spatial extension of the source C1.

In order to compare the X-ray distribution with radio synchrotron emission, the X-ray images on gray scale are overlaid with the 4850 MHz radio contours in Figure 1. The X-ray sources at the north coincide with the radio-bright region and the southern X-ray shell with a fainter radio arc. The X-ray morphology in general bears close resemblance to the radio on large scales, but the X-ray emission in the proximity of the region R2 appears to anticorrelate with the radio emission. The DR4, brightest radio region at the southeast, is quite dim in the X-ray band. It is noticeable that there are enhancements of radio emission possibly associated with the hard sources C1 and C2.

The second (Thompson et al. 1995) and third (Hartman et al. 1999) EGRET catalog report somewhat different positions for the unidentified γ -ray source inside γ Cygni. In Figure 1*c* we superimpose their 95% confidence error contours which are approximated as circles.

Whereas Brazier et al. (1996) reported a point-like X-ray source RX J2020.2+4026 by ROSAT close to the remnant center and within the EGRET error circle, no point sources were detected there by our *ASCA* observations. The flux of RX J2020.2+4026, estimated to be $\sim 4 \times 10^{-14}$ ergs cm $^{-2}$ s $^{-1}$ assuming a photon index of 2, is indeed below the sensitivity of our observation. In §4.3 we discuss a possible connection between the hard X-ray sources and the EGRET unidentified γ -ray emission.

3.2. X-ray Spectra

For the purpose of spectroscopic studies of the X-ray emissions associated with the γ Cygni SNR, contaminating emission that is overlapping the remnant must be taken into account adequately because the line of sight toward γ Cygni passes along the Orion-Cygnus spiral arm. Because of the lack of a blank field in our observations, we analyzed four *ASCA* archive data in neighboring fields (Field 1–4 in Table 1) to estimate the X-ray emission at the γ Cygni field unrelated to the SNR itself. For each field, the GIS spectrum is obtained by integrated over the central detector region with a radius of $20'$ after eliminating resolved sources. Each spectrum is subtracted by the high-latitude blank-sky spectrum as a sum of the cosmic X-ray background and the instrumental background. Figure 3 shows the resulting spectra in the 1.2–2.5 keV and 3.5–8 keV band, after the correction for the integration sky area. We find similar energy spectra from these neighborhood fields, except for Field 2 where the Galactic latitude is highest and the Galactic column density is lowest as compared with the other fields. Once Field 2 is excluded, field-to-field variations of spectral data in the soft band are found to be insignificant. The hard 3.5–8 keV spectrum of the southern field of γ Cygni is in agreement with those of Field 3 and 4 within their statistical uncertainties. Consequently, we consider that Field 3 and 4 provide us a good approximation of the contaminating emission that should be subtracted from the spectral data of γ Cygni. Since no bright sources are found in the *ASCA* data of Field 4, we have chosen Field 4 as “background” field.

We derive energy spectra of regions R1–R3 and clumps C1 and C2. The clump spectra are extracted from the circular regions of a radius of $6'$. We exclude photons falling within $6'$ radius centered on C1 and C2 from the spectrum of the region R1. Each accumulated on-source spectrum is subtracted by the “background” Field 4 spectrum that is extracted from an identical detector region to each on-source data. To improve statistics, spectra of two GIS detectors are always added. Background-subtracted spectra of R1/R3 and C2 are shown in Figure 4 and Figure 5, respectively. Several emission lines of Mg K ($\simeq 1.4$ keV) and Si K ($\simeq 1.9$ keV) are evident in every spectra, indicative of thin thermal plasma with a typical temperature of ≈ 1 keV. Remarkably, the spectrum of C2 exhibits very flat continuum emission above 3 keV. There are known errors in the calibration of the conversion of the photon energies to the pulse invariant channels of the GIS detector below the xenon-L edge of 4.8 keV. In the following spectral fitting, an artificial energy shift of -50 eV to each applied model is introduced to alleviate these errors (Buote 1999).

We have first attempted to fit the 0.7–8 keV spectrum of R3 by a thin thermal plasma model (Mewe, Gronen-

schild, & Oord 1985; Liedahl et al. 1990) in which collisional equilibrium ionization (CEI) is realized. Photoelectric absorption along the line of sight is taken into account using the cross-sections from Morrison & McCammon (1983). Elemental abundances are fixed to the solar values of Anders & Grevesse (1989) throughout this paper unless otherwise mentioned. The CEI plasma model cannot give an acceptable fit owing to a large discrepancy between the actual data and the model between Mg and Si K emission lines. Even when the abundances of alpha elements Ne, Mg, Si, S, and Fe are individually allowed to vary ranging from 0.1 to 10 solar, the spectral data cannot be described properly. In order to model emission line features, we take account of the effects of non-equilibrium ionization (NEI; Itoh 1979) by adopting a plasma emission code based on Masai (1994). In an NEI plasma, degree of ionization and consequently line emissivities depend on the ionization timescale $n_e t$, where n_e represents the electron density and t the passage time after shocked. The NEI plasma model yields an acceptable fit with a reduced $\chi^2(\text{d.o.f.}) = 1.19(26)$. The best-fit temperature and ionization timescale with 1σ errors are $kT_e = 0.76_{-0.09}^{+0.10}$ keV and $n_e t = 5.8_{-1.4}^{+1.2} \times 10^{10}$ cm $^{-3}$ s, respectively.

We found the R1 spectrum, as compared with R3, shows distinctive features, namely a strong emission at $\simeq 0.9$ keV and a hard continuum above 3 keV. The former is consistent with the fact that R1 is very bright particularly in the 0.7–1 keV energy band; the latter could be contamination by the hard sources C1 and C2. Regarding the spectral fit of R1, we include helium-like neon (Ne IX) $K\alpha$ line (0.923 keV), in addition to the CEI plasma model that predominantly describes the 1–3 keV emission. The CEI plasma plus Ne IX line model, however, cannot give a statistically acceptable fit, owing to residuals by the hard continuum. Then, by adding power-law as a third component to describe the hard continuum, we obtain an acceptable fit for the R1 spectrum as summarized in Table 2. The best-fit temperature is $kT_e = 0.56_{-0.05}^{+0.03}$ keV; the photon index of the power-law component is $\Gamma = 1.2_{-0.8}^{+1.1}$.

The spectrum of the region R2 is fitted by a CEI plasma model alone. The simple model yields an acceptable fit with the temperature of $kT_e = 0.53 \pm 0.07$ keV, which is in complete agreement with the value obtained for the region R1.

The spectral data of the clump C2 indicate the presence of a hard continuum emission in the 3–8 keV energy band. The hard emission is seen in the spectrum of C1 as well. As the case of R1, we employ a three-component model comprised of the Ne IX line (0.92 keV), CEI thermal plasma, and power-law spectrum. We find that a good fit cannot be obtained if we omit the power-law component. We fitted the three-component model to the 0.7–8 keV spectral data of the clumps C1 and C2, by freezing the plasma temperature to the best-fit value of the region R1 and attenuating all components with a common absorption column of $N_H = 0.84 \times 10^{22}$ cm $^{-2}$ that is also obtained for R1. The power-law components are found to be very flat; the best-fit photon indices are $\Gamma = 1.5 \pm 0.5$ and 0.8 ± 0.4 for C1 and C2, respectively. Instead of adding a power-law, we also attempted to add a thermal bremsstrahlung component to model the high-energy part of the C2 spectrum. The 90% lower-limit on the temperature of the thermal

bremsstrahlung emission is set to be $kT_e = 5.8$ keV.

4. DISCUSSION

4.1. Estimation of SNR Distance and Age

Higgs et al. (1977) derived the distance to γ Cygni as 1.8 ± 0.5 kpc based on the Σ - D relation which is a statistical property of the radio brightness of SNRs. Landecker, Roger & Higgs (1980) estimated as 1.5 ± 0.5 kpc and pointed out the progenitor of the γ Cygni remnant was possibly a member of the Cyg OB9 association at 1.2 ± 0.3 kpc. The absorbing column density provides additional information about the distance. Maeda et al. (1999) reported Wolf-Rayet binary V444 Cyg located close to the γ Cygni sky field is attenuated by the interstellar column density of $N_H = (1.1 \pm 0.2) \times 10^{22}$ cm $^{-2}$, similar to the γ Cygni remnant. Thus, we expect the distance to γ Cygni is probably close to the distance to V444 Cyg, 1.7 kpc. In view of these arguments, we take the distance $D = 1.5$ kpc as most probable value.

The X-ray distribution of the region R3 shows clear arc-like morphology along the outer boundary of the shell structure observed at radio frequencies. The X-ray spectrum was modeled by a single temperature thermal emission with the solar abundance. These features are indicative of a thin thermal plasma in the immediate postshock region of the primary blast wave propagating through the interstellar matter.

Assuming the equipartition between the shocked electrons and ions and Rankine-Hugoniot jump conditions for a strong shock, the electron temperature is related to the shock velocity v_s as $kT_e = (3/16)\mu m_p v_s^2$, where $\mu = 0.6$ is a mean mass per particle in units of the proton mass m_p . The best-fit value of $kT_e = 0.76_{-0.09}^{+0.10}$ keV corresponds to the shock velocity $v_s = 800_{-60}^{+50}$ km/s.

Provided that the remnant is in the Sedov adiabatic expansion phase, the age of γ Cygni can be estimated to be $\tau_{\text{age}} = (2/5)R/v_s$, where R is the radius of the supernova shock front. Given the angular radius of $\theta \simeq 30'$, we have the physical radius $R = D\theta \simeq 13.5D_{1.5}$ pc, where $D_{1.5}$ is the distance in units of 1.5 kpc. Thus, we obtain an age estimate of $\tau_{\text{age}} \simeq 6600D_{1.5}$ yr.

4.2. Signatures of Shock-Cloud Interaction

On the basis of the H I line emission and absorption toward the γ Cygni SNR, Landecker, Roger & Higgs (1980) suggested that the supernova explosion took place in the slab of an interstellar cloud oriented north to southeast. The soft (1–3 keV) X-ray emission “belt” from north to southeast appears to agree fairly well with the spatial distribution of the H I line features. A possible scenario explaining this coincidence is that the X-ray emission belt is due to thermal evaporation of clouds (White & Long 1991) as a consequence of the collision between the supernova blast wave and the dense clouds. The supernova shock may expand into a cavity produced by progenitor stellar winds, and then encounter the cavity wall comprised of the clouds (Chevalier 1999).

We found the possible evidence of the strong emission line of helium-like Ne from the R1 spectrum. The X-ray map in the 0.7–1 keV band suggests clumpy nature of the Ne IX line emission. The upper limit for the hydrogen-like

Ne line intensity is found to be 6.7% of the helium-like intensity. This gives an upper limit of 0.24 keV for the temperature of plasma emitting the Ne IX line if we assume ionization equilibrium state. The low-temperature and clumpy appearance are indicative of the shock-cloud interactions at the northern part of the remnant.

The hard sources C1 and C2 reside in the northern region where the shock-cloud interaction is likely to occur. Therefore, we identify the hard sources with shocked dense cloudlets. This speculation may be encouraged by the presence of high-velocity H I cloudlets with a density of 10–100 cm $^{-3}$ and an apparent radius of 4'–6' in the south-east of the remnant (Landecker, Roger & Higgs 1980). Let us calculate the density of plasma that is responsible for the derived Ne flux $I_{\text{Ne}} \sim 6(0.8) \times 10^{-3}$ photons cm $^{-2}$ s $^{-1}$ of the clump C1(C2) with reasonable parameters. Given a temperature of 0.1 keV and a spherical volume of an angular radius of 2' (assuming distance $D = 1.5$ kpc), we have the density $n \approx 60(8)$ cm $^{-3}$ by using the Ne line emissivity of Mewe, Gronenschild, & Oord (1985), in agreement with the typical density of H I cloudlets.

4.3. On the Origin of Hard X-ray Emission

An important finding of our observations is the clumpy hard X-ray emissions from the regions C1 and C2 (hereafter, HXC – the hard X-ray clump). We found that C2 has an extended structure with an effective radius of about 4'. The HXC components are extremely hard and characterized by a power-law with $\Gamma \sim 0.8$ –1.5. As we argued above, it is likely the HXC originates in shocked dense cloudlets with a gas density between 10 and 100 cm $^{-3}$.

The thermal-bremsstrahlung interpretation of the high-energy part of the C2 spectrum requires very high temperature ($kT_e > 5.8$ keV). Since the shocks of an evolved SNR are not sufficiently energetic to heat the gas to such temperatures, the nonthermal origin of the hard X-ray emission seems a more favorable option. The synchrotron radiation, the inverse-Compton scattering, and the nonthermal bremsstrahlung of shock-accelerated electrons are three natural production mechanisms of hard X-rays. The overall flux of the HXC in the 2–10 keV interval is estimated as $F_X \simeq 4.5 \times 10^{-12}$ ergs cm $^{-2}$ s $^{-1}$, which corresponds to the source luminosity $L_X \simeq 1.2 \times 10^{33}D_{1.5}^2$ ergs s $^{-1}$.

The nonthermal luminosity of this SNR peaks at high energy γ -rays, if the association with the EGRET source is real. The γ -ray spectrum measured by EGRET is shown in Figure 6, together with the HXC spectrum. The observed photon flux of the EGRET source is translated into a luminosity of $L_\gamma \simeq 1.4 \times 10^{35}D_{1.5}^2$ ergs s $^{-1}$ (100 MeV–2 GeV) for the photon index 2.1. The reported positions of the EGRET γ -ray source 2EG J2020+4026 and/or 3EG J2020+4017 do not coincide exactly with the HXC. However the large systematic errors in the EGRET position, which strongly depend on the chosen diffuse γ -ray emission model (Hunter et al. 1997), do not allow certain conclusions concerning the location of the γ -ray production region. Therefore it is interesting to test whether the HXC can be a counterpart of the unidentified GeV γ -rays source on theoretical ground.

4.3.1. Coulomb Cooling and Nonthermal Bremsstrahlung

The emission region of the HXC is supposed to be the dense cloudlet engulfed by the supernova blast wave, and

therefore the density is probably high ($n \sim 10\text{--}100 \text{ cm}^{-3}$). Below we assume that accelerated electrons are continuously injected in the HXC, by the accelerator(s) being located either outside or inside the HXC. Possible internal accelerator could be the secondary shocks generated by the interaction between the primary blast wave and the dense cloudlets. Indeed, Bykov et al. (2000) considered electron acceleration at a slow shock (the order of 100 km/s) transmitted inside a dense cloudlet. A tail shock could be formed behind the cloudlets (Jones & Kang 1993) as well, although an efficient particle acceleration at the tail shock is not obvious. On the other hand, the external accelerator should be the primary shock of the SNR.

The energy spectrum of accelerated electrons depends on the acceleration mechanism, the discussion of which is beyond the scope of this paper. For simplicity we assume the electron production rate in momentum space is described by a single power-law function $Q(p) \propto p^{-\kappa}$. Such a function implies power-law distributions of electrons also in the kinetic energy space, although in the non-relativistic and ultrarelativistic regimes the power-law indices are different, namely $Q(E) \propto E^{-(s+1)/2}$ at $E \ll m_e c^2$ while $Q(E) \propto E^{-s}$ at $E \gg m_e c^2$, where $s = \kappa + 2$. In the case of diffusive shock acceleration at the shock front, according to the standard model (Bell 1978; Blandford & Eichler 1987), the spectral index is determined by the compression ratio of the shock as $s = (r+2)/(r-1)$. For strong shocks with $r \sim 4$ the spectral index is close to 2.

For simplicity we suppose that the electrons are effectively trapped in HXC; thus the present-day electron spectrum is formed by accumulation of freshly accelerated (or arriving from external accelerators) electrons during the entire history of the HXC. If the energy-losses can be neglected, the electron spectrum becomes $N(E) = \tau_{\text{age}} Q(E)$, where the age of the accelerator is approximated by the age of γ Cygni, i.e. $\tau_{\text{age}} \simeq 7000 \text{ yr}$. It is valid, however, only in the intermediate energy region, typically between 300 MeV to 10 GeV, where the bremsstrahlung dominates the radiative losses. Indeed, the characteristic lifetime of electrons against the bremsstrahlung losses, $\tau_{\text{br}} = E/(-dE/dt)_{\text{br}} \simeq 4.3 \times 10^7 (n/10 \text{ cm}^{-3})^{-1} \text{ yr}$ is considerably larger than the age of γ Cygni as long as the gas density does not exceed $6 \times 10^4 \text{ cm}^{-3}$.

The high density and presumably strong magnetic field in the HXC make, however, the cooling processes crucial in the formation of the electron spectrum at low and very high energies. The relevant cooling processes are the Coulomb (or, in the neutral gas, ionization) losses for low-energy electrons and the synchrotron losses for high-energy electrons. The inverse-Compton losses could be omitted if the magnetic field in HXC exceeds $10 \mu\text{G}$. Also, it should be noticed that even in case of significant bremsstrahlung losses ($\tau_{\text{br}} \leq \tau_{\text{age}}$), the process does not modify the electron spectrum.

Below several hundreds MeV, the energy losses of electrons are dominated (independent of the gas density) by the Coulomb losses (see e.g. Hayakawa 1969). The cooling time of electrons due to the Coulomb interactions is given by (Rephaeli 1979)

$$\tau_{\text{cou}} = \frac{E}{(3/2)n_e c \sigma_{\text{T}} (m_e c^2) \beta^{-1} \ln \Lambda} \quad (1)$$

$$= 4.3 \times 10^3 \beta \left(\frac{n}{10 \text{ cm}^{-3}} \right)^{-1} \left(\frac{E}{\text{MeV}} \right) \text{ yr}, \quad (2)$$

where σ_{T} is the Thomson cross-section, c is the velocity of light, E and β are the kinetic energy and the velocity of nonthermal electrons in units of c , m_e is the electron mass, and $\ln \Lambda$ is the Coulomb logarithm which is set to be 40. Equating τ_{cou} and τ_{age} gives the break energy E_{cou} , ‘‘Coulomb break’’, below which the electron spectrum is flattened:

$$E_{\text{cou}} \sim 1.6 \left(\frac{n}{10 \text{ cm}^{-3}} \right) \left(\frac{\tau_{\text{age}}}{7000 \text{ yr}} \right) \text{ MeV}, \quad (3)$$

where we use the approximation of $\beta \sim 1$. At energies below E_{cou} the Coulomb losses significantly modify the acceleration spectrum, $N(E) = \tau_{\text{cou}}(E)Q(E)$; namely, at relativistic energies, $N(E) \propto E^{-s+1}$.

The differential energy spectrum of the bremsstrahlung emission from these electrons is calculated as (see e.g. Blumenthal & Gould 1970)

$$I(\varepsilon) \simeq \int dE N(E) c \beta \left(n_{\text{H}} \frac{d\sigma_{e\text{H}}}{d\varepsilon} + n_{\text{He}} \frac{d\sigma_{e\text{He}}}{d\varepsilon} + n_e \frac{d\sigma_{ee}}{d\varepsilon} \right), \quad (4)$$

where n_{H} , n_{He} , and n_e are hydrogen, helium, and electron number densities, respectively, and $d\sigma/d\varepsilon$ is the differential cross-section for emitting a bremsstrahlung photon in the energy interval ε to $\varepsilon + d\varepsilon$. We adopt ratios $n_{\text{He}}/n_{\text{H}} = 0.1$ and $n_e/n_{\text{H}} = 1.2$. In the ultrarelativistic regime the electron-electron bremsstrahlung becomes comparable to the electron-proton bremsstrahlung. Since the bremsstrahlung cross-section is in inverse proportion to the emitted photon energy, $d\sigma/d\varepsilon \propto \varepsilon^{-1}$, and only slightly (logarithmically) depends on the electron energy in the relativistic regime, the bremsstrahlung photon spectrum almost repeats the power-law spectrum of parent electron distribution of $N(E) = kE^{-\alpha}$, i.e. $I(\varepsilon) \propto \varepsilon^{-\alpha}$ if $\alpha \geq 1$. Then, we should expect a broken power-law spectrum with $I(\varepsilon) \propto \varepsilon^{-s}$ at $\varepsilon \geq E_{\text{cou}}$, and $I(\varepsilon) \propto \varepsilon^{-s+1}$ at $\varepsilon < E_{\text{cou}}$ in the relativistic domain. The energy spectrum of bremsstrahlung photons is essentially determined by the gas density and the age. Below the ‘‘Coulomb break’’, for any reasonable acceleration index of $s \leq 2.5$, we see a hard differential spectrum with a photon index less than 1.5. It should be stressed that, for the electron spectrum harder than E^{-1} ($E^{-1/2}$ in the non-relativistic case), the bremsstrahlung photons obey a standard ε^{-1} type spectrum. In the *ASCA* energy band, we should always expect the standard spectrum.

4.3.2. Synchrotron Radiation

The synchrotron cooling time of electrons in the magnetic field B is given by

$$\tau_{\text{syn}} = \frac{\gamma m_e c^2}{(4/3) c \sigma_{\text{T}} U_B \gamma^2} \quad (5)$$

$$= 1.2 \times 10^3 \left(\frac{B}{10^{-5} \text{ G}} \right)^{-2} \left(\frac{E}{10^{14} \text{ eV}} \right)^{-1} \text{ yr}, \quad (6)$$

where γ is the electron Lorentz factor and $U_B = B^2/(8\pi)$ is the energy density of the magnetic field. Equating τ_{syn} and τ_{age} gives the break energy E_{syn} above which the electron spectrum is steepened:

$$E_{\text{syn}} \sim 18 \left(\frac{B}{10^{-5} \text{ G}} \right)^{-2} \left(\frac{\tau_{\text{age}}}{7000 \text{ yr}} \right)^{-1} \text{ TeV}. \quad (7)$$

Thus if the maximum energy of electrons exceeds E_{syn} , we should expect a break in the electron spectrum. In particular, in the case of power-law acceleration spectrum, the loss-steepened spectrum has a power-law form $N(E) = \tau_{\text{syn}}(E)Q(E) \propto E^{-s-1}$.

The average synchrotron photon energy radiated by an electron with energy of E_{14} (in 10^{14} eV) in the field B_{-5} (in 10^{-5} G) is $\epsilon \sim 1.6B_{-5}E_{14}^2$ keV. Then, the break energy E_{syn} at which the synchrotron lifetime is balanced with the SNR age is translated into the synchrotron photon energy of $\epsilon_{\text{syn}} \sim 50 (B/10^{-5}\text{G})^{-3}(\tau_{\text{age}}/7000\text{yr})^{-2}$ eV, above which noticeable spectral steepening should appear. Therefore the observed flat X-ray spectrum up to 10 keV would require unrealistically small magnetic field in the HXC region, $B \leq 2 \mu\text{G}$.

Furthermore, it is easy to show that in the case of acceleration of electrons inside HXC, independent of the strength of the magnetic field, the cut-off energy in the synchrotron spectrum cannot exceed a few eV. Indeed, if the maximum energy of accelerating electrons is limited by the synchrotron losses, the balance between the acceleration and cooling timescales determines the maximum electron energy. The timescale of the first-order Fermi acceleration in the Bohm diffusion limit is given by

$$\tau_{\text{acc}} \sim \frac{r_{LC}}{v_s^2} \quad (8)$$

$$= 3.1 \times 10^5 \left(\frac{B}{10^{-5}\text{G}} \right)^{-1} \left(\frac{v_s}{100\text{ km/s}} \right)^{-2} \left(\frac{E}{10^{14}\text{eV}} \right) \quad (9)$$

where $r_L = m_e\gamma/(eB)$ is the Larmor radius of electrons and v_s is the shock velocity. Equating τ_{syn} in equation (5) and τ_{acc} gives the maximum energy $E_m \sim 6.2 (B/10^{-5}\text{G})^{-1/2}(v_s/100\text{ km/s})$ TeV, and its characteristic photon energy is $\epsilon_m \sim 3.8 (v_s/100\text{ km/s})^2$ eV that is independent of the magnetic field strength. Hence, regardless of the magnetic field strength, the first-order Fermi acceleration mechanism cannot explain the extremely flat X-ray spectrum by synchrotron radiation, unless the shock speed exceeds 5000 km/s. The latter condition obviously cannot be satisfied in γ Cygni.

4.3.3. Inverse-Compton Emission

The hard X-rays could be produced also by inverse-Compton (IC) scattering of seed photons off relativistic electrons. In the γ Cygni SNR, the cosmic microwave background (CMB) radiation dominates over other ambient photon fields like the diffuse Galactic infrared/optical radiation and the infrared emission from shock-heated dust (Gaisser, Protheroe, & Stanev 1998).

Relativistic electrons which boost the CMB photons up to X-rays also emit synchrotron radiation in the radio band. Characteristic energies of synchrotron photon ϵ_{syn} and IC photon ϵ_{ic} (in keV) produced by the same electrons are related as (e.g. Aharonian, Atoyan, & Kifune 1997)

$$\epsilon_{\text{syn}} \simeq 0.7 \times 10^{-7} \epsilon_{\text{ic}} B_{-5} \text{ eV} \quad (10)$$

for the CMB seed field. The ratio of the spectral power $f(\epsilon) \equiv \epsilon^2 \times I(\epsilon)$ of the IC X-ray emission to the synchrotron emission at the relevant radio frequency is

$$\frac{f_{\text{ic}}(\epsilon_{\text{ic}})}{f_{\text{syn}}(\epsilon_{\text{syn}})} = \frac{U_{\text{CMB}}}{U_B}, \quad (11)$$

where $U_{\text{CMB}} = 0.25 \text{ eV cm}^{-3}$ is the energy density of the CMB radiation. The spectral power of the observed radio emission from the whole remnant, in the frequency range from 408 MHz to 4.8 GHz (Wendker, Higgs, & Landecker 1991; Higgs et al. 1977) is well described as

$$f_{\text{radio}}(\epsilon) = 5 \times 10^{-12} \left(\frac{\epsilon}{10^{-5} \text{ eV}} \right)^{0.5} \text{ ergs cm}^{-2}\text{s}^{-1}. \quad (12)$$

Since almost 60% of the radio flux comes from the southeast of γ Cygni, from equation (10) and (11) we find that the IC spectral power cannot exceed $1.7 \times 10^{-14} \epsilon_{\text{ic}}^{0.5} B_{-5}^{-1.5} \text{ ergs cm}^{-2}\text{s}^{-1}$. This upper-limit is less than 1% of the flux of the hard X-ray emission detected. Thus, the IC radiation hardly can explain the flux of HXC, unless the magnetic field is extremely weak ($< 1 \mu\text{G}$).

4.3.4. Nonthermal Bremsstrahlung X/ γ -radiation

The nonthermal bremsstrahlung from the accelerated electrons is a natural source of the HXC flux, because the shocked dense cloudlets act as an effective target for energetic electrons. Because of Coulomb interactions the high density gas leads to significant hardening of low-energy electrons below the ‘‘Coulomb break’’, giving rise to the standard ϵ^{-1} type bremsstrahlung spectrum at the X-ray band, which perfectly agrees with the *ASCA* data. The bremsstrahlung spectrum above the ‘‘Coulomb break’’ essentially repeats the acceleration spectrum of electrons. For the given spectral index of accelerated electrons, the ratio of the X- and γ -ray fluxes depends only on the ‘‘Coulomb break’’ energy which in its turn depends on the gas density and the age of the accelerator.

In Figure 6 we show the results of numerical calculations for two sets of parameters which describe the gas density and the acceleration spectrum of electrons, by assuming the electron bremsstrahlung is responsible for both the *ASCA* hard X-ray and the EGRET γ -ray fluxes. For the electron spectrum with the acceleration index $s = 2.1$, the best fit is achieved for a gas density of $n = 34 \text{ cm}^{-3}$. A steeper acceleration spectrum with $s = 2.3$ requires larger gas density, $n = 130 \text{ cm}^{-3}$. Note that the adopted acceleration spectra are consistent with the reported radio spectral index $\alpha = 0.5 \pm 0.15$. We also suppose an exponential cutoff in the electron spectrum at 10 TeV.

If the electron distribution with $s = 2.3(2.1)$ extends beyond GeV energies, for the magnetic field 10^{-5} G the calculated radio flux density amounts to about 10%(60%) of the measured radio flux density integrated over the whole remnant. Furthermore, if the electron distribution extends beyond TeV, we found the bremsstrahlung spectrum with $s = 2.1$ exceeds the Whipple upper-limit, whereas the spectral index of $s = 2.3$ is still in agreement with the Whipple data. Meanwhile both combinations of model parameters satisfactorily fit the spectral shape and the absolute flux of hard X-rays. The ignorance of energy losses of electrons would lead to significantly steeper X-ray spectra, and would also result in overproduction of absolute X-ray fluxes (dotted curves in Figure 6). Note that the main contribution to X-rays comes from relatively high energy electrons with energies close to 10 MeV for the electron index $s = 2.3$.

Because of poor angular resolution, the EGRET measurements do not provide a clear information about the site(s) of production of high energy γ -rays. Nevertheless,

it is likely that only a part (perhaps, even only a small part) of the reported high energy γ -ray fluxes originates in the HXC region. The γ -ray fluxes could be suppressed by assuming lower gas densities. Indeed, such an assumption would lead to the shift of the ‘‘Coulomb break’’ energy in the electron spectrum to lower energies, and the predicted high energy γ -ray spectra would appear significantly below the reported EGRET fluxes (a solid curve in Figure 6).

A more likely candidate for production of the bulk of high energy γ -rays is the region called DR4 from which most of the radio emission emerges. A massive cloud with a density of $\sim 300 \text{ cm}^{-3}$ occupying $\sim 5\%$ of the SNR volume has been suggested to exist in the vicinity of DR4 to explain the γ -ray flux (Pollock 1985). Actually the EGRET error circle reported is somewhat away from the HXC but closer to the DR4. A density of $\sim 300 \text{ cm}^{-3}$ is higher than the upper limit density of the HXC. Such high gas density implies a high (about 50 MeV) ‘‘Coulomb break’’ energy in the electron spectrum, and therefore considerable suppression of X-ray flux. This could naturally explain the lack of noticeable hard X-ray fluxes from the DR4 region which is bright in radio and possibly γ -rays.

Finally, we briefly discuss the power consumption due to the rapid Coulomb losses. For the gas density of about 100 cm^{-3} in the HXC, the X-ray flux is produced predominantly by electrons with energies of about 10 MeV. The X-ray flux is roughly proportional to the product of the gas density and the number of relativistic electrons, because the relativistic bremsstrahlung cross-section depends only logarithmically on the electron energy. On the other hand, the Coulomb energy loss rate of relativistic electrons, $dE/dt \propto E/\tau_{\text{cou}}$, is proportional to the gas density and almost independent of the electron energy. Therefore the energy loss rate of the bulk of the X-ray emitting electrons can be uniquely determined by the X-ray luminosity. The measured X-ray luminosity, $L_X \simeq 1.2 \times 10^{33} D_{1.5}^2 \text{ ergs s}^{-1}$, can be converted to the energy loss rate of $L_e \sim 5 \times 10^{37} D_{1.5}^2 \text{ ergs s}^{-1}$. The energy released in relativistic electrons is roughly estimated as $W_e \sim \tau_{\text{age}} L_e \sim 10^{49} D_{1.5}^2 \text{ ergs}$. This enormous energy deposition due to Coulomb collisions would heat the emission region of the HXC. Subsequently the heat would be radiated away in the far-infrared band by molecular line emission, if the gas is comprised of molecules. The observed infrared luminosity of γ Cygni (Saken, Fesen, & Shull 1992) is comparable to the energy loss rate estimated above. On the other hand, if the emission region of the HXC are predominantly shock-ionized plasmas, the deposited energies by the accelerated electrons would heat up the plasmas.

5. SUMMARY AND CONCLUSION

The X-ray emissions emerging from the γ Cygni SNR are found to be complex. Spatial and spectral studies of the X-ray data reveal the presence of four components: (1) limb-brightened thermal emission with a temperature of $\simeq 0.8 \text{ keV}$; (2) widespread emission with a temperature of $\simeq 0.6 \text{ keV}$ aligned from north to southeast bounded

by the radio-bright regions; (3) strong emission lines from Ne IX ions in the vicinity of the northern bright-radio region; (4) clumpy hard emissions, which is best described by unusually hard power-law spectral distribution with a photon index $\Gamma \simeq 0.8\text{--}1.5$.

The limb-brightened component is considered to be thermal plasma emission from the immediate postshock region of the SNR blast wave that is propagating through the interstellar medium. The temperature gives the age estimate of $\tau_{\text{age}} \sim 6600 \text{ yr}$ based on the Sedov evolution of the remnant. The soft X-ray emissions from north to southeast are likely to be caused by the interaction between the supernova shock and the cavity wall comprised of ambient clouds. In particular, the intense neon line emission would be attributable to the low-temperature plasma generated by the shock-cloud interaction.

The extremely hard X-ray emission of the HXC is naturally explained by the nonthermal bremsstrahlung from the loss-flattened electron distribution. By assuming that the HXC is a counterpart of the EGRET unidentified γ -ray source 3EG J2020+4017, we estimate the density of the emission region to be $\sim 130 \text{ cm}^{-3}$, for the electron index 2.3. The bremsstrahlung interpretation requires very large Coulomb energy loss rate of $\sim 5 \times 10^{37} \text{ ergs s}^{-1}$ and consequently the total amount of the energy loss of $\sim 10^{49} \text{ ergs}$, regardless of the gas density and the energy of electrons responsible for the hard X-radiation. Given the limited energy budget of γ Cygni, it is more comfortable to attribute this huge energy release to the acceleration at the HXC region, rather than to assume that the electrons are supplied by external accelerators. Otherwise, the energy requirement would be increased by an order-of-magnitude or more, unless we assume very specific arrangement of external accelerators around the HXC region.

If the HXC region contributes only a fraction of the EGRET high energy γ -ray flux, the gas density estimate of 130 cm^{-3} should be considered as an upper limit. All accelerated electrons are presumed to be trapped inside the HXC volume. However, it may be possible that high-energy ($\geq 100 \text{ MeV}$) electrons effectively escape from the HXC, and later interact with very dense clouds resulting in high energy γ -rays and synchrotron radio emission, but without noticeable X-radiation. The spatial structures of the HXC will be comprehensively studied by our forthcoming *Chandra* observation. The origin of the γ -ray emission from γ Cygni will eventually be tested by the future *Gamma-Ray Large Area Space Telescope (GLAST)* mission.

We thank Dr. L. Drury for his critical comment concerning the interpretation of the site of electron acceleration. Y.U. thanks Dr. M. Ishida for stimulating discussions and his advice on the *ASCA* data analysis, and also wish to thank all the members of the *ASCA* team. The work of Y.U. was supported in part by the Research Fellowships of the Japan Society for the Promotion of Science for Young Scientists.

REFERENCES

- Aharonian, F.A., Atoyan, A.M., & Kifune, T. 1997, *MNRAS*, 291, 162
- Aharonian, F.A., Drury, L.O'C., & Völk, H.J. 1994, *A&A*, 285, 645
- Anders, E., & Grevesse, N. 1989, *Geochim. Cosmochim. Acta*, 53, 197
- Bell, A.R. 1978, *MNRAS*, 182, 147
- Blandford, R. & Eichler, D. 1987, *Phys. Rep.*, 154, 1
- Blumenthal, G.R., & Gould, R.J. 1970, *Rev. Mod. Phys.*, 42(2), 237
- Brazier, K.T.S., Kanbach, G., Carraminana, A., Guichard, J., & Merck, M. 1996, *MNRAS*, 281, 1033
- Buckley, J.H., et al. 1998, *A&A*, 329, 639
- Buote, D.A. 1999, *MNRAS*, 309, 685
- Burke, E.B., Mountain, R.W., Daniels, P.J., Cooper, M.J., and Dorat, V.S. 1994, *IEEE Trans. Nucl. Sci.*, 41, 375
- Bykov, A.M., Chevalier, R.A., Ellison, D.C., & Uvarov, Yu.A. 2000, *ApJ*, 538, 203
- Chevalier, R.A. 1999, *ApJ*, 511, 798
- Combi, J.A., Romero, G.E., & Benaglia, P. 1998, *A&A*, 333, L91
- Combi, J.A., Romero, G.E., Benaglia, P., & Jonas, J.L. 2001, *A&A*, 366, 1047
- Downes, D., & Rinehart, R. 1966, *ApJ*, 144, 937
- Drury, L.O'C., Aharonian, F.A., & Völk, H.J. 1994, *A&A*, 287, 959
- Esposito, J.A., Hunter, S.D., Kanbach, G., & Sreekumar, P. 1996, *ApJ*, 461, 820
- Gaisser, T.K., Protheroe, R.J., & Stanev, T. 1998, *ApJ*, 429, 219
- Green, D.A. "A Catalogue of Galactic Supernova Remnants (2000 August version)", Mullard Radio Astronomy Observatory, Cavendish Laboratory, Cambridge, UK
- Hartman, R.C., et al. 1999, *ApJS*, 123, 79
- Hayakawa, S. 1969, *Cosmic Ray Physics*, Wiley-Interscience
- Higgs, L.A., Landecker, T.L., & Roger, R.S. 1977, *AJ*, 82, 718
- Hunter, S.D., et al. 1997, *ApJ*, 481, 205
- Itoh, H. 1979, *PASJ*, 31, 541
- Jones, T.W., & Kang, H. 1993, *ApJ*, 402, 560
- Landecker, T.L., Roger, R.S., & Higgs, L.A. 1980, *A&AS*, 39, 133
- Liedahl, D.A., Kahn, S.M., Osterheld, A.L., & Goldstein, W.H. 1990, *ApJ*, 350, 37
- Maeda, Y., Koyama, K., Yokogawa, J., & Skinner, S. 1999, *ApJ*, 510, 967
- Makishima, K., et al. 1996, *PASJ*, 48, 171
- Masai, K. 1994, *ApJ*, 437, 770
- Mewe, R., Gronenschild, E.H.B.M., & van den Oord, G.H.J. 1985, *A&AS*, 62, 197
- Morrison, R., McCammon, D. 1983, *ApJ*, 270, 119
- Naito, T., Yoshida, T., Mori, M., & Tanimori, T. 1999, *Astron. Nachr.*, 320, 205
- Pollock, A.M.T., 1985, *A&A*, 150, 339
- Rephaeli, Y., 1979, *ApJ*, 227, 364
- Saken, J.M., Fesen, L.A., & Shull, M. 1992, *ApJS*, 81, 715
- Sturmer, S.J. & Dermer, C.D. 1995, *A&A*, 293, L17
- Thompson, D.J., et al. 1995, *ApJS*, 101, 259
- Wendker, H.J., Higgs, L.A., & Landecker, T.L. 1991, *A&A*, 241, 551
- White, R.L., & Long, K.S. 1991, *ApJ*, 373, 543
- Zhang, X., Zheng, Y., Landecker, T.L., & Higgs, L.A. 1997, *A&A*, 324, 641

FIG. 1.— (a)–(c): *ASCA* GIS X-ray images (*gray scale*) of the γ Cygni supernova remnant in (a) 0.7–1 keV, (b) 1–3 keV, and (c) 4–7 keV energy bands. Two GIS detectors (GIS2, GIS3) are summed. The brightness level indicated at the top of the images is in units of the surface brightness of the cosmic X-ray background of the relevant energy interval. Radio contour map (NRAO 4.85 GHz: 7' FWHM) is superposed on the *ASCA* images. A central part of strong emission around an H II region called γ Cygni nebula at southeast is blanked from the radio map. Also shown are the EGRET 95% confidence error circles (*dotted circle*: 2EG J2020+4026, *thick circle*: 3EG J2020+4017).

FIG. 2.— The GIS radial count rate profile of the clump C2 in the 3–10 keV energy band. A histogram represents the simulated radial profile of a point source. Estimated background level is taken from the southern part of the remnant.

FIG. 3.— A comparison between the energy spectra integrated over the GIS field-of-view in the 1.2–2.5 keV energy band (*top*) and the 3.5–8 keV band (*bottom*); the south γ Cygni (*filled circle*), Field 1 (*open circle*), Field 2 (*rectangle*), Field 3 (*diamond*), and Field 4 (*triangle*).

FIG. 4.— The GIS energy spectra extracted from the regions R1 (*filled circle*) and R3 (*open circle*), with linear scale. The R3 spectrum is multiplied by a factor of 0.3 for display purpose only. The curves show best-fit models, folded through the response function of the instrument. The bottom panels plot the residuals of data compared with the thermal emission models.

FIG. 5.— The GIS energy spectra extracted from the clump C2 (*filled circle*), where the background data are taken from the Field 4. The curve shows only the thermal component of the best-fit model, folded through the response function of the instrument. The bottom panel plots the residuals of data compared with the thermal component. Also shown is the high-energy part of the C2 spectrum whose background data are taken from the southern portion of γ Cygni (*open circle*); the high-energy continuum is hardly affected by the choice of the background data.

FIG. 6.— Broadband spectral power of the γ Cygni SNR. The range of the power-law fit of the hard X-ray component is shown together with γ -ray data (≥ 100 MeV) of 2EG J2020+4026 taken from Esposito et al. (1996) and the Whipple TeV upper limit from Buckley et al. (1998). The bremsstrahlung photon spectra from the loss-flattened electron distribution are calculated for the electron index $s = 2.1$ and the gas density $n = 34 \text{ cm}^{-3}$ (*long-dashed line*), $s = 2.3$ and $n = 130 \text{ cm}^{-3}$ (*dashed line*), and $s = 2.3$ and $n = 10 \text{ cm}^{-3}$ (*solid line*). The *dotted lines* show the bremsstrahlung spectra corresponding to the acceleration spectra of electrons, i.e. ignoring the Coulomb losses of electrons.

TABLE 1
SUMMARY OF THE *ASCA* ARCHIVE FIELDS NEAR THE γ CYGNI SNR

Field	Target	Coordinate (l, b)	Distance ^a (deg)
γ Cygni ^b	2EG J2020+4026 2	(77°:92, 2°:22)	0.0
Field 1	V444 Cyg	(76°:66, 1°:43)	1.5
Field 2	NGC 6888	(75°:55, 2°:42)	2.4
Field 3	GRO J2019+37	(75°:45, 0°:61)	2.9
Field 4	GEV 2035+4213	(81°:22, 1°:02)	3.5

^aAngular distance from (l, b) = (77°:92, 2°:22).

^bThis pointing covers the southern part of the γ Cygni SNR.

TABLE 2
 RESULTS OF SPECTRAL FITS TO THE *ASCA* DATA OF γ CYGNI

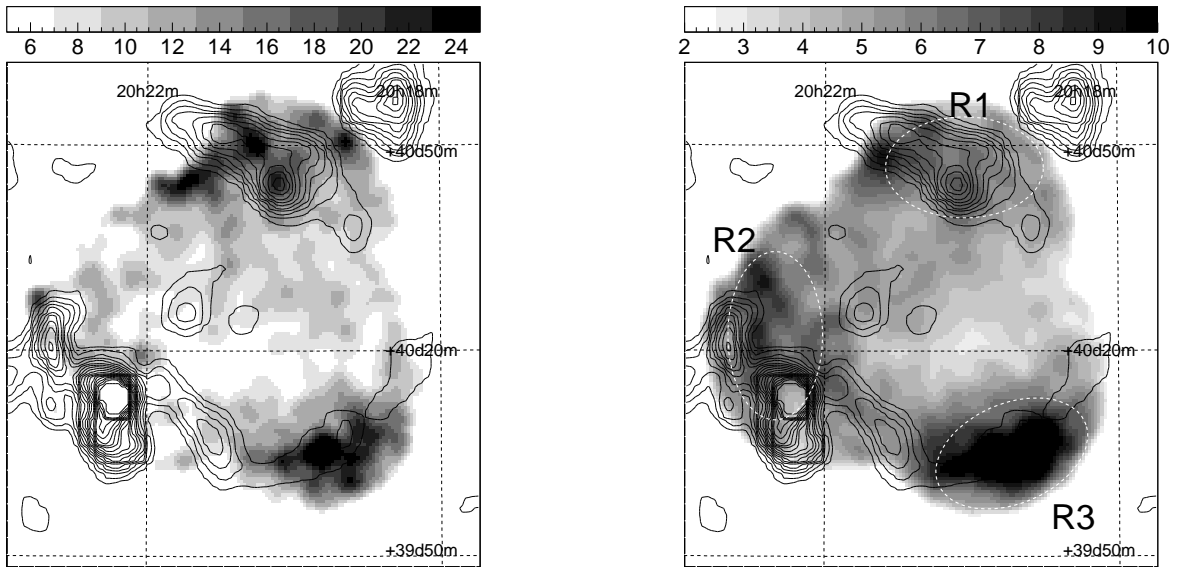
Parameter	R3	R2	R1	C2	C1
Power Law:					
Photon Index Γ	$1.2^{+1.1}_{-0.8}$	0.8 ± 0.4	1.5 ± 0.5
$F_{2-10 \text{ keV}}^a$	$1.8^{+0.6}_{-0.5}$	$0.98^{+0.21}_{-0.20}$	$1.7^{+0.5}_{-0.4}$
Thermal Plasma:					
kT (keV)	$0.76^{+0.10}_{-0.09}$	0.53 ± 0.07	$0.56^{+0.03}_{-0.05}$	0.56 fixed	0.56 fixed
EM (10^{12} cm^{-5}) ^b	$3.5^{+1.0}_{-0.7}$	$3.0^{+1.5}_{-0.8}$	$1.3^{+0.3}_{-0.5}$	0.47 ± 0.02	$0.97^{+0.07}_{-0.08}$
$n_e t$ ($10^{10} \text{ cm}^{-3} \text{ s}$)	$5.8^{+1.2}_{-1.4}$
Neon Line:					
I_{Ne} ($10^{-3} \text{ ph cm}^{-2} \text{ s}^{-1}$) ^c	$7.9^{+4.5}_{-5.2}$	$0.83^{+0.03}_{-0.04}$	$5.5^{+1.1}_{-1.0}$
Photoelectric Absorption:					
N_{H} (10^{22} cm^{-2})	1.1 ± 0.1	$1.2^{+0.2}_{-0.1}$	$0.84^{+0.10}_{-0.23}$	0.84 fixed	0.84 fixed
χ^2_ν (ν)	1.19(26)	0.80(14)	0.96(34)	1.21(40)	1.25(14)

^aUnabsorbed flux (2–10 keV) in units of $10^{-12} \text{ ergs cm}^{-2} \text{ s}^{-1}$.

^bEmission Measure: $\int n_e n_H dV / 4\pi D^2$.

^cPhoton flux of helium-like Ne K emission line (0.92 keV).

Note. — Best-fit values and their 1σ errors.



(a) 0.7-1 keV

(b) 1-3 keV

FIG. 1.— GIS images

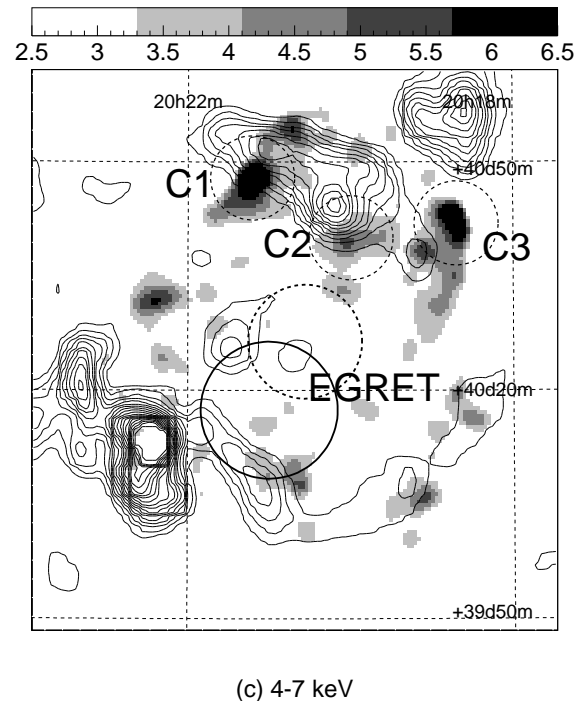


FIG. 1.— GIS images

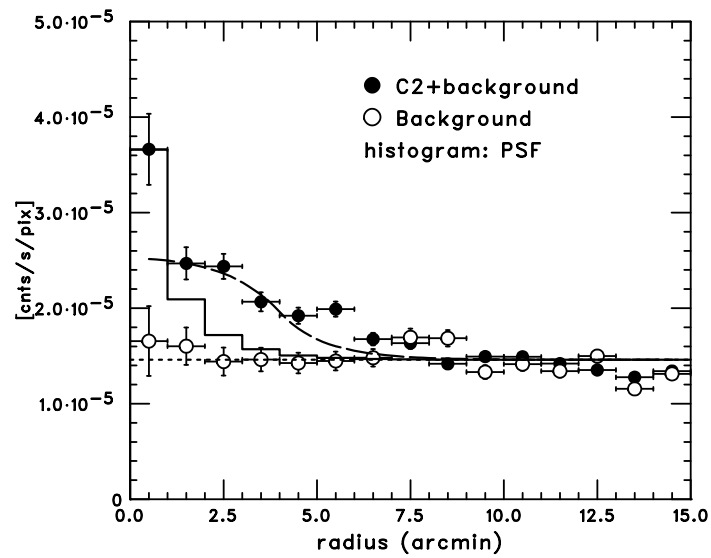


FIG. 2.— Radial Profile of C2

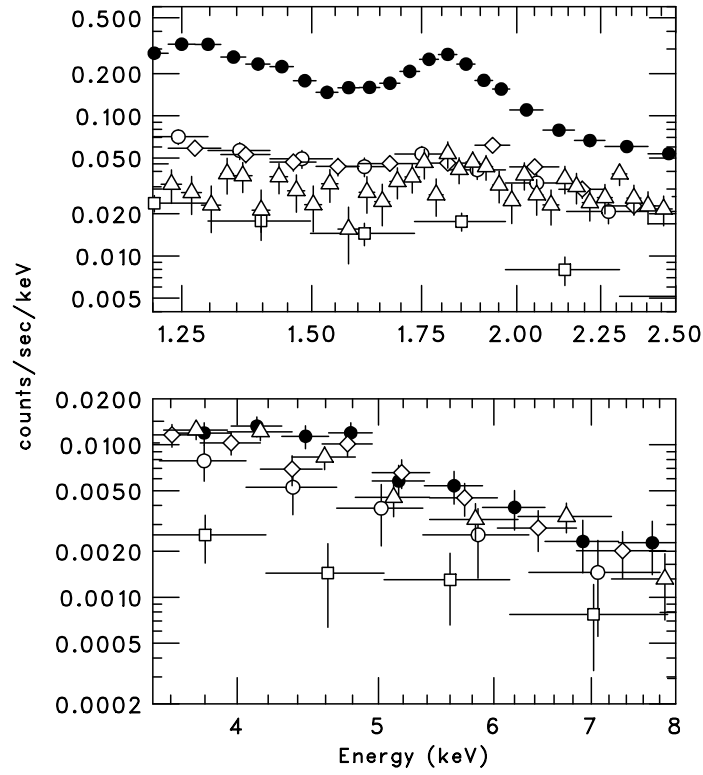


FIG. 3.— Background Fields

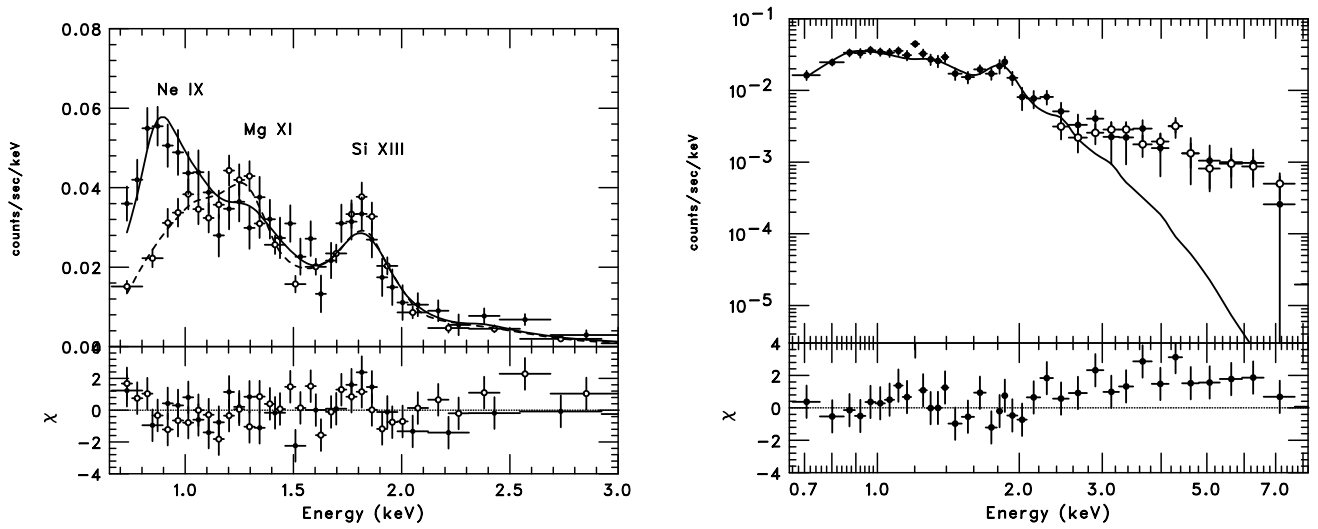


FIG. 4-5.— GIS spectrum R1/3(left) C2(right)

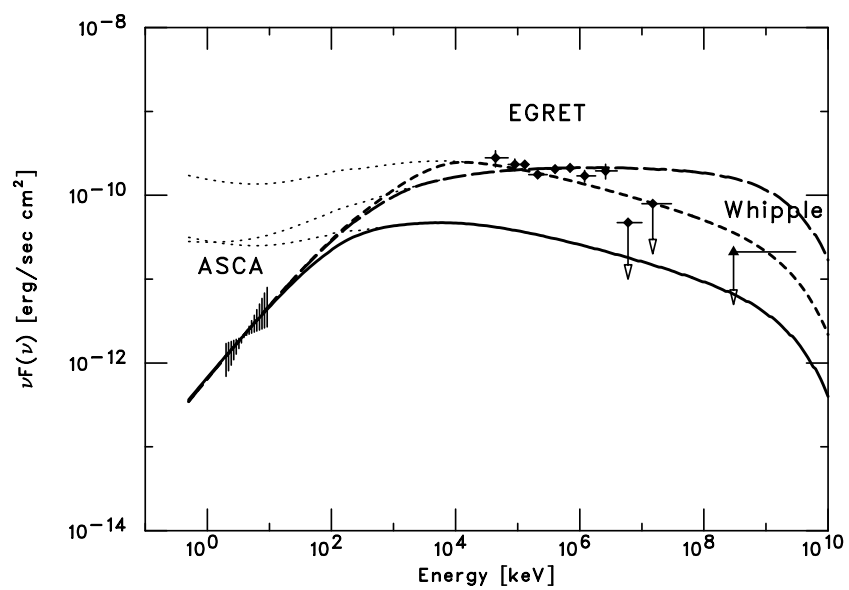


FIG. 6.— Broadband spectrum